

PAPER

## Electron emission from fluorene ( $C_{13}H_{10}$ ) upon 3.5 MeV/u $Si^{8+}$ ion impact: double differential distributions

To cite this article: Chandan Bagdia *et al* 2021 *J. Phys. B: At. Mol. Opt. Phys.* **54** 155202

View the [article online](#) for updates and enhancements.

### You may also like

- [Double differential electron emission in ionization of Coronene by fast ions](#)  
Shubhadeep Biswas, C Champion and Lokesh C Tribedi
- [Phase, AC conductivity and dielectric properties of Indeno\[1,2-b\]fluorene-6,12 dione thin film as a function of frequency and temperature](#)  
A El-Denglawey, Saleem I Qashou, A A A Darwish *et al.*
- [Molecular origin of photostability for fluorene-based donor–acceptor type photovoltaic polymers](#)  
Hiroki Ozaki, Tatsuya Fukushima, Yasuko Koshiha *et al.*






**IOP | ebooks™**

Bringing together innovative digital publishing with leading authors from the global scientific community.

Start exploring the collection—download the first chapter of every title for free.

# Electron emission from fluorene (C<sub>13</sub>H<sub>10</sub>) upon 3.5 MeV/u Si<sup>8+</sup> ion impact: double differential distributions

Chandan Bagdia<sup>1</sup> , Anuvab Mandal<sup>1</sup>, Madhusree Roy Chowdhury<sup>1</sup>, Shamik Bhattacharjee<sup>1</sup>, M Nrisimha Murty<sup>1</sup>, Deepankar Misra<sup>1</sup> , Christophe Champion<sup>2</sup>, László Gulyás<sup>3</sup>, Philippe F Weck<sup>4</sup> and Lokesh C Tribedi<sup>1,\*</sup> 

<sup>1</sup> Department of Nuclear and Atomic Physics, Tata Institute of Fundamental Research, 1, Homi Bhabha Road, Colaba, Mumbai-400005, India

<sup>2</sup> CELiA, Centre Lasers Intenses et Applications, Université de Bordeaux, CNRS-CEA, F-33400, Talence, France

<sup>3</sup> Institute of Nuclear Research of the Hungarian Academy of Sciences (ATOMKI), H-4001 Debrecen, Hungary

<sup>4</sup> Sandia National Laboratories, Albuquerque, New Mexico 87185, United States of America

E-mail: [lokesh@tifr.res.in](mailto:lokesh@tifr.res.in) and [ltribedi@gmail.com](mailto:ltribedi@gmail.com)

Received 26 April 2021, revised 13 July 2021

Accepted for publication 3 August 2021

Published 25 August 2021



CrossMark

## Abstract

We have studied the electron emission from one of the polycyclic aromatic hydrocarbon (PAH) molecules namely, fluorene (C<sub>13</sub>H<sub>10</sub>), upon 3.5 MeV/u Si<sup>8+</sup> ion impact. The experimentally measured absolute double differential cross sections (DDCS) are compared with the continuum distorted wave-eikonal initial state (CDW-EIS) model and the first Born approximation including correct boundary conditions (CB1). The measurements are carried out in the ejected e<sup>-</sup>-energy range of 1 eV–400 eV and in the angular range of 20°–160°. We have obtained the single differential and the total cross sections (TCSs) of e<sup>-</sup>-emission as well. The CB1 calculation largely underestimates the data. The CDW-EIS model, which is applied for the PAH molecule for the first time, provides an overall better agreement with the double differential, single differential and TCS data. The DDCS data for fluorene has also been compared with that for CH<sub>4</sub> molecule, at a few angles. The forward–backward angular asymmetry shows a relatively flatter distribution compared to the theoretical predictions. The contribution due to the giant plasmon resonance could not be clearly observed except a mild indication in the asymmetry parameter. The angular distribution of the carbon KLL Auger electron cross section shows certain variations. The study of the KLL hyper-satellite component indicates the double K-ionization cross section is about 8.6% of the single K-ionization one.

Keywords: polycyclic aromatic hydrocarbon molecules, electron spectroscopy, ion–molecule collision, continuum distorted wave-eikonal initial state model, electron double differential cross sections, single differential cross sections, highly charged ions, fluorene

(Some figures may appear in colour only in the online journal)

\* Author to whom any correspondence should be addressed.

## 1. Introduction

The polycyclic aromatic hydrocarbon (PAH) molecules have attracted special attention in the last two decades due to its predicted abundance in the interstellar medium (ISM) [1]. The PAH molecules are planar, made up of carbon and hydrogen atoms, consisting of multiple benzoidal rings. These molecules have a large diversity in terms of the number of carbon atoms and their size, from the simplest one with two benzoidal rings,  $C_{10}H_8$  (naphthalene), to one of the largest synthesized PAH,  $C_{222}H_{42}$ , having 91 benzoidal rings [2, 3].

A few of the leading questions driving the current research involving PAH molecules are, how such big and complex molecules are produced in the ISM, how do they survive (stability) in the harsh interstellar environment and what are the various emission/absorption features arising upon interaction with cosmic rays and their implication in the observed absorption and emission spectra from the ISM [1, 4–12]. To understand the above-stated problems there have been intense experimental and theoretical investigations by researchers from different fields, such as astronomy and astrophysics, atomic and molecular physics, quantum chemistry and condensed matter physics, etc. Particularly from a molecular physics perspective, the various molecular properties of PAH molecules are being explored by studying the interaction of these molecules with ions and electrons, as these are an integral part of the interstellar environment [13]. Hence, the ionization and fragmentation of PAH molecules upon interaction with these radiations are subject of the recent studies [14–24]. However, most of the existing studies using ion beams deal with the fragmentation of PAH molecules and to the best of our knowledge, the measurement of the electron emission from PAH molecules upon ion impact is very scarce [23, 24].

Moreover, the double differential cross section of electron emission from atoms and molecules upon ion impact provides a stringent test to the various theoretical models in addition to the information about underlying processes. Although the multi-electronic, multi-particle description of the molecule poses a difficult challenge to the theory, various theoretical models have been successful to a great extent in modeling the electron emission from atoms and small molecules in such collisions [25–32]. Significant progress has also been made for large bio-molecules e.g. RNA–DNA base molecules [33–38]. However, there is only one report presenting a comparison between *ab initio* quantum mechanical calculation with the experimental data for electron emission from PAH molecules upon ion impact [24].

The PAH molecules have delocalized  $\pi$ -electron cloud around covalently bonded carbon cage. It has been predicted that these electrons can oscillate collectively about the C cage upon external perturbation [39–42]. Such collective oscillation is also known as the giant plasmon excitation and it predominantly decays via the electron emission channel. Hence, it is important to study the electron emission from the PAH molecule upon external perturbation. Recently, the signature of such collective excitation, in the electron emission channel, upon ion impact has been reported for coronene ( $C_{24}H_{12}$ ) molecules [23].

In this work, we have studied the electron emission upon ion impact from the fluorene ( $C_{13}H_{10}$ ) molecules, another member of the PAH family with a lesser number of C-atoms. The fluorene molecule has two benzoidal rings connected by a pentagonal ring having 12  $\pi$ -electrons whereas the coronene molecule has seven benzoidal rings with 24  $\pi$ -electrons. The absolute double differential cross sections (DDCS) for electron emission (e-DDCS) from fluorene molecules upon 3.5 MeV/u  $Si^{8+}$  ion impact have been measured. The measured data have been compared with the first Born approximation with correct boundary conditions (CB1) model calculations [43] and the continuum distorted wave eikonal initial state (CDW-EIS) model calculations [44]. The e-DDCS measurements have been performed in the electron energy range of 1–400 eV and in the angular range of  $20^\circ$ – $160^\circ$ . The  $e^-$ -emission spectrum for fluorene has also been compared with those for smaller molecules,  $CH_4$  in a few cases under the same collision.

## 2. Experimental details and data analysis

In this section, we briefly describe the experimental setup used, the target preparation and the data analysis procedure. The schematic of the experimental setup used has been shown in figure 1.

### 2.1. Experimental setup

The experiment is performed using 98 MeV  $Si^{8+}$  ion beams from 14 MV Pelletron accelerator at TIFR, Mumbai. The beam is collimated using two sets of four jaw slits kept 1 m apart. The well collimated beam is made to pass through a 4 mm diameter collimator at the entrance of the high vacuum scattering chamber. The base vacuum of  $1 \times 10^{-7}$  mbar is achieved inside the scattering chamber using a 2000 l  $s^{-1}$  turbomolecular pump backed by a rotary pump. The electrostatic hemispherical electron energy analyzer is placed inside the chamber on a rotatable turntable. The radii of the inner and outer hemispheres of the spectrometer are 2.5 cm and 3.5 cm respectively. The resolution of the electron spectrometer is 6% of the electron energy. It is important to take precautions to reduce any stray electric and magnetic fields in the chamber which can affect the electron trajectory specifically that of the low energy electrons. Two layers of the  $\mu$ -metal sheet are used inside the chamber to reduce the earth's magnetic field to a level of  $\sim 10$  mG. Good cleanliness inside the chamber is maintained. A pre-acceleration voltage of 6 V is applied at the entrance and exit slit of the spectrometer to increase the collection efficiency of the low energy electrons [45]. The energy analyzed electrons are detected using a channel electron multiplier (CEM) detector mounted at the end of the spectrometer. The CEM is biased at 2400 V by applying +2500 V and +100 V on the back and the front of the CEM, respectively. The front voltage is chosen such that the detection efficiency of the CEM is high and constant ( $\sim 0.85$ ) for the electron energy range of 100–600 eV. The number of projectile ions is calculated by measuring the charge collected in a long Faraday cup using a current integrator. The LabVIEW based data acquisition

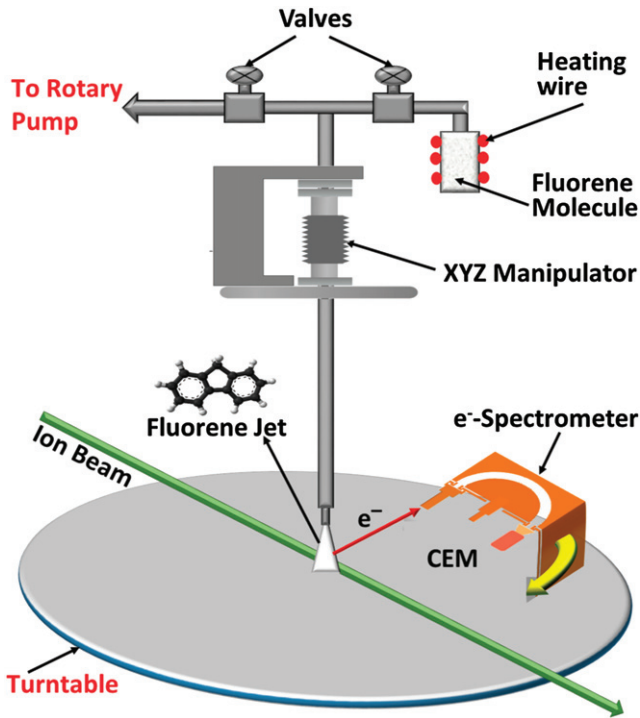


Figure 1. Schematic of the experimental setup.

system is used to scan the voltages on hemispheres and collect the data.

### 2.2. Target preparation

The experiment is performed using the effusive vapor jet of fluorene molecules formed by heating the commercially available powder of fluorene [46]. The vapor pressure of fluorene at room temperature of 27°C is high enough ( $1.12 \times 10^{-3}$  mbar [47]) so that in the chamber vacuum of  $1 \times 10^{-7}$  mbar it can be evaporated without heating. We found that a little bit of heating is required to increase the density. The heating has been done from outside and the desired vapor density has been achieved by heating the powder to about 63°C. The aspect ratio of the nozzle used is 10. The height of the nozzle from the beam is kept at 4 mm. The molecule holder has been placed outside the chamber as shown in figure 1. It has been connected to the jet using stainless steel tubes. The jet has been mounted on the XYZ manipulator for the alignment purpose. A complete overlap of the effusive jet with the ion beam was ensured. The molecular holder has been pumped using an additional rotary pump to remove the water content in the powder.

### 2.3. Data analysis

The relative DDCCS of electron emission at a particular electron energy and an emission angle is obtained by subtracting the background electron count from that obtained with the target. To measure the absolute DDCCS, the target density of the fluorene molecule is to be known. In the case of an effusive vapor jet target, the density is dependent upon the jet profile and the vapor pressure. We calculate the jet profile using Scoles'

formalism and convolute it with the spectrometer solid-angle-path-length [48]. The vapor pressure is a strong function of temperature and measuring the temperature precisely inside the molecule holder is often difficult. Hence we use a technique for absolute normalization based on the carbon KLL Auger yield. As the C-KLL Auger emission is an inner shell process, we assume that the KLL-Auger cross section (per C-atom) for methane and fluorene will be the same. Hence, we have performed an independent experiment with CH<sub>4</sub> gas with a static pressure. The detail measurements of the DDCCS at different angles were carried out. The single differential cross section (SDCCS) in electron energy ( $d\sigma/d\varepsilon_e$ ) was deduced for CH<sub>4</sub> gas using the first principle. Finally, the total C-KLL Auger cross section was obtained from the SDCCS. The normalization factor has been obtained by taking the ratio of total absolute C-KLL Auger cross section for CH<sub>4</sub> to that of relative C-KLL Auger cross section (per carbon atom) for the fluorene molecule. The detailed process for normalization and absolute cross section measurement for vapor jet targets can be found in [34, 49].

## 3. Theoretical models

### 3.1. CB1

As clearly detailed in one of our previous works [30], the DDCCS have been calculated within the 1st Born approximation (FBA) with initial and final wavefunctions verifying correct boundary conditions (CB1) (see [50]). More explicitly, the DDCCS relative to the emission solid angle  $\Omega_e$  as well the electron energy  $\varepsilon_e$ , denoted  $\frac{d^2\sigma}{d\Omega_e d\varepsilon_e}$ , were here obtained from the numerical integration of the triply differential cross sections (TDCS)  $\frac{d^3\sigma}{d\Omega_s d\Omega_e d\varepsilon_e}$  over the scattering angle  $\Omega_s$ . Within the FBA–CB1 framework, the TDCS are related to the transition matrix element between the initial state labeled 'i' and the final state labeled 'f' expressed by

$$T_{if} = \langle \Psi_f(\vec{r}_0, \vec{r}_1) | V(\vec{r}_0, \vec{r}_1) | \Psi_i(\vec{r}_0, \vec{r}_1) \rangle, \quad (1)$$

where the interaction potential  $V(\vec{r}_0, \vec{r}_1)$  can be simply written by using the well-known 'frozen core' approximation which reduces the present multi-electron problem to a one-active-electron problem as

$$V(\vec{r}_0, \vec{r}_1) = \frac{-Z_p}{|\vec{r}_0 - \vec{r}_1|} + \frac{Z_p}{r_0}, \quad (2)$$

where  $\vec{r}_1$  is the position vector of the active electron with respect to the framework center and  $\vec{r}_0$  is the position vector of the incident projectile with respect to the framework center.  $Z_p$  refers to the projectile charge. In this context, it is worth noting that the molecular orbitals of the target were here expressed in terms of linear combinations of atomic orbitals—all centered to a common origin—provided by the quantum-mechanical description given by the GAUSSIAN 09 software at the restricted Hartree–Fock/3–21G level of theory [51]. Thus, the TDCS and therefore the DDCCS, were calculated for each molecular orbital of the impacted target, the global TDCS being simply obtained by summing-up all the shell contributions.

### 3.2. Continuum distorted wave-eikonal initial state

The cross-sections have also been calculated within the CDW-EIS. The CDW-EIS model is a first order distorted wave method which proved to be a very successful for describing atomic collisions at medium and high impact energies [52, 53] and its extension to molecular collisions have been provided in [44, 54]. To the best of our knowledge, this is the first time, that it has been applied for the PAH molecule. The model is constructed within the framework of active-electron approximation, where only one electron is considered as active during the collision, while all the remaining electrons have been described as frozen spectators. As it is known for particles interacting with Coulomb force, the approaching or receding projectile ion, having velocity  $\mathbf{v}$  and charge  $Z_p$ , distorts the electronic state of the target even at infinite separations [52, 55]. The distortions are neglected for the motions of heavy nuclei and they are considered only for the treatment of the active electron in the present semi-classical treatment. The model was extended for multi electronic targets by including numerically calculated wave functions in both initial and final channels [56]. The effect of the projectile on the electronic state is taken into account by using eikonal distorted wave function

$$\chi_i^+(\mathbf{x}, t) = e^{-i\varepsilon_i t} \Phi_i(\mathbf{x}) E_v^*(\mathbf{s}, \eta_i) \quad (3)$$

for the initial channel, and by the Coulomb distorted wave function

$$\chi_k^-(\mathbf{x}, t) = e^{-i\varepsilon_k t} \Phi_k^-(\mathbf{x}) D_p(\mathbf{s}, \eta_p) \quad (4)$$

for the final channel.  $\Phi_i(\mathbf{x})$  and  $\Phi_k(\mathbf{x})$  denote the unperturbed initial and final electronic orbitals, respectively,  $\mathbf{x}$  stands for the position vector of the active electron with respect to the target center and  $\mathbf{k}$  is the momentum for the ejected electron. The distortion factors  $E_v^*(\mathbf{s}, \eta_i)$  and  $D_p(\mathbf{s}, \eta_p)$  are given by

$$E_v(\mathbf{s}, \eta_i) = (v_s + \mathbf{v} \cdot \mathbf{s})^{i\eta_i} \quad (5)$$

and

$$D_p(\mathbf{s}, \eta_p) = e^{\pi\eta_p/2} \Gamma(1 + i\eta_p) {}_1F_1(-i\eta_p, 1, -i(ps + \mathbf{p} \cdot \mathbf{s})), \quad (6)$$

respectively, where  $\eta_i = Z_p/v$ ,  $\eta_p = Z_p/p$ ,  $\mathbf{p} = \mathbf{k} - \mathbf{v}$ ,  $\mathbf{s} = \mathbf{x} - \mathbf{R}$ ,  $\mathbf{R}$  is the position vector of the projectile referring to the target center, and  ${}_1F_1$  is the confluent hypergeometric function. Beyond the correct asymptotic behavior, the Coulomb distortion enables to describe the active electron moving in the combined electric field created by the projectile and target core, which is referred to as two center effects in the literature [53].

The fluorene molecule has 44 orbital filled with two electrons. Each molecular orbital is constructed as a linear combination of atomic orbitals centered on the constituting individual C and the H atoms. The continuum orbital ( $\Phi_k(\mathbf{x})$ ), is described on a spherically averaged potential created by the nuclei and the passive electrons. Considering only the valence orbitals and performing the single center expansion of the mule-center molecular wave functions, still requires a considerable computational effort that we wanted to avoid in the present treatment. Therefore, our description of the molecule relies on a simpler, known as complete neglect of differential

overlap (CNDO) approximation [57]. The method starts from the Hartree–Fock equation, adopt a minimal basis sets, replace the core electrons by an effective charge, and totally neglects the monoatomic differential overlap. Therefore only the gross feature of the electron–electron interaction is included. As a result the molecular orbitals can be represented in terms of the corresponding atomic orbitals of the constituent atoms (i.e. a Mulliken population analysis [58]) and the DDCS for a given  $j$ th molecular orbital is obtained as

$$\frac{d^2\sigma_j}{d\varepsilon_e d\Omega_e} = \sum_i \xi_{j,i} \frac{d^2\sigma_i}{d\varepsilon_e d\Omega_e}, \quad (7)$$

where  $\xi_{j,i}$  is the effective number of electrons relative to the  $i$ th atomic orbitals of the C or H atoms ( $i = 1s, 2s, 2p$ ). Molecular orbital energies and the  $\xi_{j,i}$  values were evaluated with the GAUSSIAN 09 software package [51]. The ground-state geometry of the molecule were optimized using the density functional theory [59] with Dunning’s correlation consistent polarized valence basis set of double- $\zeta$  quality [60], and the population analysis were performed at the Hartree–Fock level using 6–31G basis sets.

The DDCS for ionization of the  $C_{13}H_{10}$  molecule is expressed as

$$\frac{d^2\sigma}{d\varepsilon_e d\Omega_e} = \sum_{j=1}^N \frac{d^2\sigma_j}{d\varepsilon_e d\Omega_e}, \quad (8)$$

where  $N$  is the number of molecular orbitals used in the description of the target. For the reliability of describing DDCS for ionization of simple molecules by impacts of energetic ions within the framework of CNDO approximation, see e.g. [61, 62].

## 4. Results and discussions

In this section, the experimentally measured energy and angular distributions of the absolute e-DDCS and the comparison with CB1 and CDW-EIS model calculations are presented. The SDCS and total cross section (TCS) of the electron emission have also been presented along with the forward–backward asymmetry of e-DDCS and the angular distribution of the C-KLL Auger electron emission.

### 4.1. Electron DDCS

We present here the measured absolute e-DDCS in the electron energy range of 1–400 eV for 12 different emission angles in the angular range of  $20^\circ$ – $160^\circ$ . We have also measured the same spectrum at  $-90^\circ$  (or  $270^\circ$ ). The consistency of the spectrum at  $\pm 90^\circ$  implies that the ion beam overlaps at the central part of the jet. Figure 2 shows the energy distribution of DDCS of electron emission at  $90^\circ$  and  $270^\circ$ . The data at both the angles match very well within experimental uncertainties, providing confidence in jet alignment.

**4.1.1. Energy distribution of DDCS.** The measured energy distributions of the absolute DDCS at fixed emission angles are plotted in figure 3. In general, for all the spectra, the cross section falls several orders of magnitude over the electron

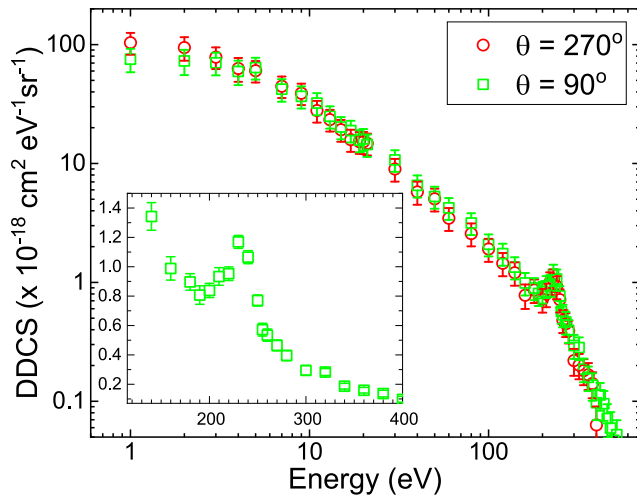


**Figure 2.** Energy distribution of the DDCS of electron emission from fluorene molecules at  $90^\circ$  and  $270^\circ$ . The zoomed in spectrum of the C-KLL Auger region is shown as an inset.

energy range of 1–400 eV. The increasing ejected electron energy can be associated with the decreasing impact parameter i.e. lower (higher) energy electrons emitted in large (small) impact parameter collisions. The lowest energy electrons in the spectrum correspond to a small momentum transfer and typically referred to as soft collision emission. The intermediate energy range electrons, arising from a closer collision, show the effect of both target and projectile interaction which is also known as two center electron emission (TCEE) in the case of ion–atom collisions. The peak at an electron energy of 240 eV in all the spectra corresponds to the C-KLL Auger electron emission resulting from the K-vacancy in the carbon atom in fluorene molecules. The expanded plot of the C-KLL region has been shown as an inset in figures 3(i) and (k). We can observe the signature of hyper-satellite as a shoulder in the C-KLL Auger peak at higher energy i.e. at  $\sim 285$  eV (see figures 3(i) and (k)). The hyper-satellite peak arises due to the double K-vacancy produced in the collision. The C-KLL Auger peak is more prominent in backward angles as compared to forward angles. It is mainly because of Coulomb continuum background is higher for small forward angles as compared to the backward angles, which will be discussed in section 4.4. The detailed discussions on the Auger electron angular distribution and the hyper-satellite have been presented in section 4.3.

In figures 3(b) and (j), the electron DDCS spectra at an angle of  $30^\circ$  and  $135^\circ$  are shown for the  $\text{CH}_4$  molecule. The DDCS spectrum for fluorene is qualitatively similar to that of  $\text{CH}_4$  although the absolute DDCS for the fluorene molecule is much higher than the  $\text{CH}_4$ . The data for  $\text{CH}_4$  is multiplied by a factor of 3, just for better display. The solid blue line and the dashed black line in figure 3 corresponds to the CDW-EIS and the CB1 calculations respectively. Overall, in terms of the absolute values, the CB1 calculation predicts the measured data reasonably well for low energy electrons ( $\leq 9$  eV), whereas it largely underestimates the data for higher energy electrons. In the low energy region, the CB1 shows small

oscillations in cross section. However, such oscillations are not physically justified. For higher energy electrons ( $\geq 11$  eV), it qualitatively reproduces the electron spectrum observed in the perpendicular direction to beam propagation i.e. for angles in the range of  $75^\circ$ – $105^\circ$ . As we go in extreme forward or backward angles the slope of the CB1 calculation is steeper than the measured data. The deviation at the higher electron energy (beyond C-KLL Auger energy) is higher for the backward angles as compared to the forward angles indicating that the CB1 calculation is overestimating the post-collision interaction (PCI), giving forward–backward asymmetry. In comparison to the CB1 calculation, the CDW-EIS model predicts the measured data reasonably well both qualitatively and quantitatively. The CDW-EIS model overestimates the data for lower energy (up to  $\sim 80$  eV) electrons. It predicts the data very well for the higher energy electrons ( $> 100$  eV). However, for the highest energy electrons (beyond C-KLL Auger peak) the deviation with the measured data increases with the larger backward angles.

The DDCS plot (figure 3) is plotted in the log–log scale and to compare the measured data with calculations more clearly, the ratio of the data to theory for eight representative angles has been plotted in figure 4. The ratio is plotted up to 150 eV. The dashed line in the plot corresponds to the ratio value of 1. The dashed-dotted (black) lines and solid (blue) lines correspond to the CB1 and CDW-EIS calculations respectively. The CB1 calculation is underestimating data for all the angles at all electron energies except in the lowest energy region ( $\leq 9$  eV) of backward angles. Whereas, the CDW-EIS model calculation overestimates the data for the low energy electrons and underestimates the data for the higher energy electrons ( $> 100$  eV) for the extreme backward angles. The deviation of CB1 calculation from measured data increases with the increasing emitted electron energy for all the angles in contrast to the CDW-EIS calculations. The ratio for CB1 varies in the range of 0.4–7.8 based on the emitted electron energy for extreme forward and backward angles. On the other hand, it varies only in the range of 0.85–3.4 for the emission angles closer to  $90^\circ$ . Therefore the overall deviation of the theory from the experiment is larger for small forward and large backward angles. The minimum deviation at  $75^\circ$ – $90^\circ$  is because for these angles the binary encounter dominates the low energy spectrum which is well reproduced by the first Born (B1) as well as CB1 calculations. For extreme forward angles, the post-collisional interaction between projectile and ejected electrons is quite strong and may not be fully accounted for in the CB1. For backward angles, the rescattering of the electron from the target nucleus is an important mechanism that is to be fully considered in the theory. As far as the ratio with the CDW-EIS is concerned the agreement with the lowest energy ( $\sim 5$  eV) electrons is excellent and the ratio is around 0.85–1 and then the deviation with the measured data increases to 0.55 around 20 eV for all the angles. For the forward and small backward angles, the deviation reduces for higher energy (80 eV–150 eV) electrons. However, for extreme backward angles, it underestimates the data by a factor of 2–2.7. The CDW-EIS takes in to account for the post-collisional interaction between the ejected electron

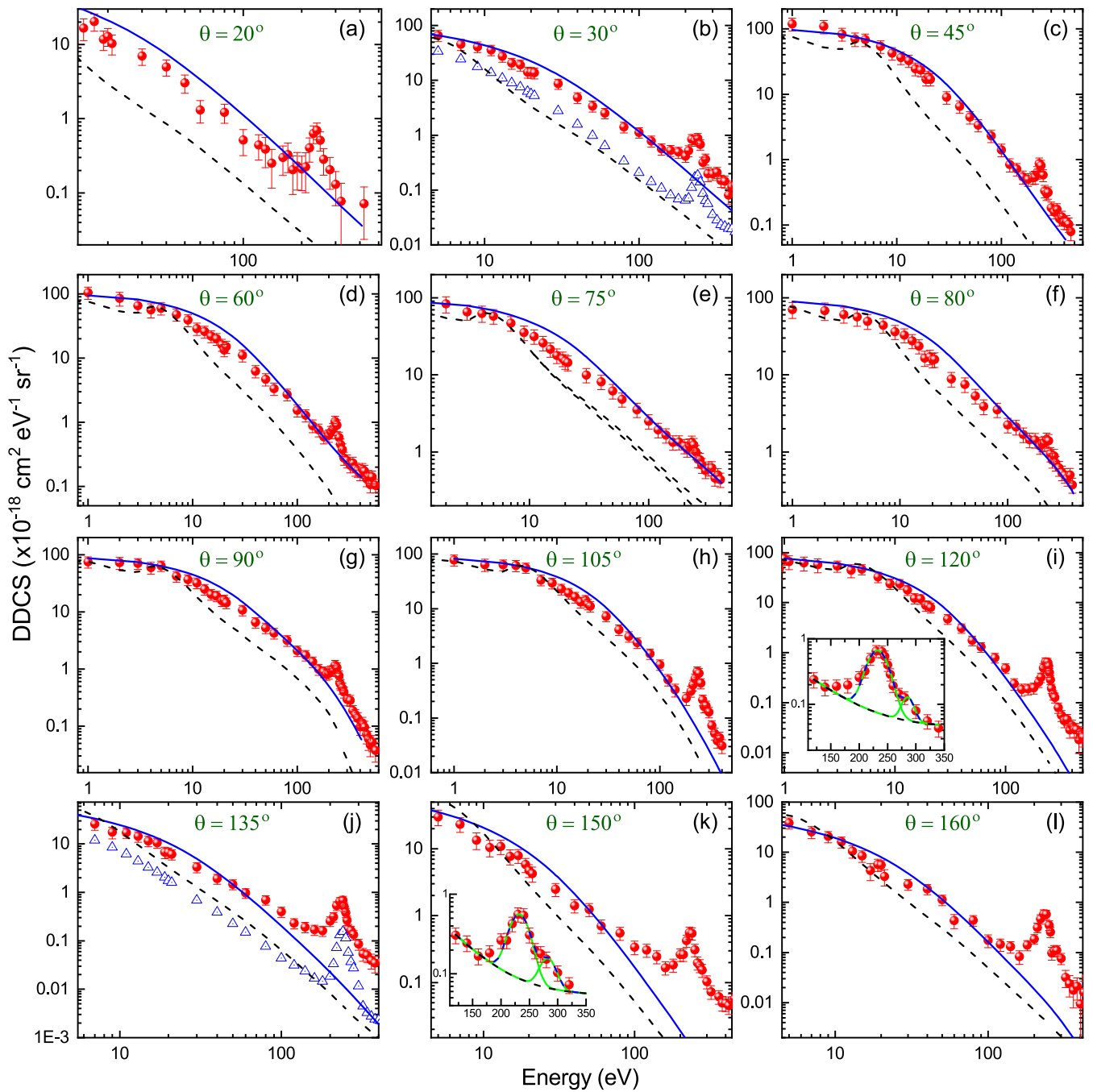


**Figure 3.** Energy distributions of DDCS of electron emission from fluorene upon 98 MeV  $\text{Si}^{8+}$  ion impact at different electron emission angles. Solid (blue) line represents CDW-EIS model calculations and dashed (black) line represents CB1 calculations. The  $\text{CH}_4$  data (triangles) is multiplied by a factor of 3. Inset in the panel (i) and (k) show the fitted curves to the Auger and hyper-satellite peaks.

and both the projectile and residual target. Hence, for the intermediate energy ( $>60$  eV) electrons, the CDW-EIS predictions are in good agreement with the data.

**4.1.2. Angular distribution of DDCS.** The angular distributions of e-DDCS at a fixed electron energy are plotted for eight different electron energies (see figure 5). The solid (blue) and dashed (black) curves in figure 5 represent the CDW-EIS and CB1 calculations respectively. The CB1 calculation underestimates the data for all energy electrons except the lowest energy

(7 eV) electrons. The deviation of the CB1 with the data for forward and backward angles increases with the emitted electron energy as it can be seen clearly in angular distributions. The CDW-EIS calculation overestimates the same for low energy electrons whereas it predicts the data very well for intermediate energies. For high energy electrons, the CDW-EIS underestimates the data in the backward angles. The typical deviation for the CB1 at  $80^\circ$  is in the range 1.1–7.3 whereas that for the CDW-EIS is in the range 0.6–1.1. A steady fall in the cross sections is observed in the case of low electron energy (7 eV and 15 eV), instead of a flat distribution which may

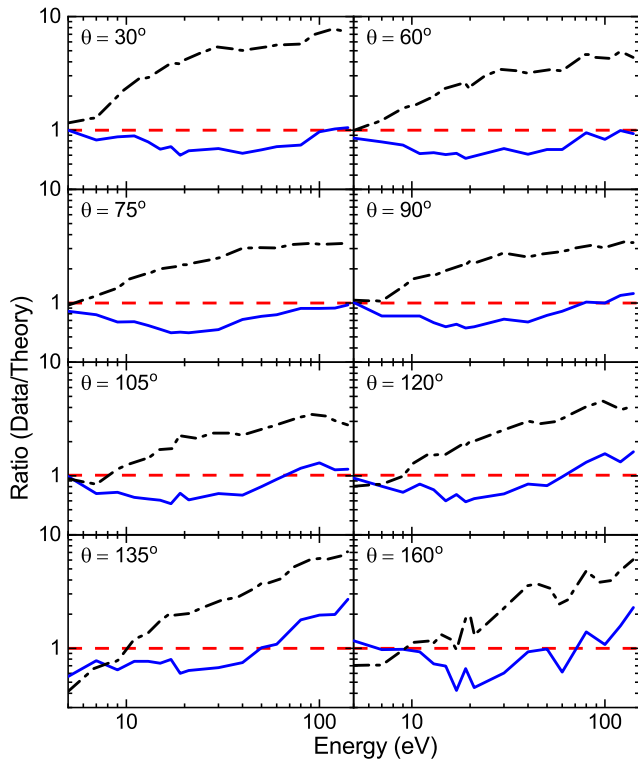


**Figure 4.** Ratio of the measured DDCS data to the CB1 (dashed-dotted black lines) and CDW-EIS (solid blue lines) calculations for different angles.

be expected in an ion–atom collision [25]. The observed fall could be associated with the molecular nature of the target. Such fall has been observed earlier for molecular targets such as coronene, uracil or H<sub>2</sub>O [24, 32, 34]. The steady fall for the case of the PAH molecule i.e. coronene has been associated with the collective excitation. Such low energy e<sup>−</sup>-emissions are dominated by a large impact parameter collision. At such distant collision, the whole molecule responds together to the electric field due to the swift ions. However, at higher energies, a peak like structure emerges near 80° which is understood in terms of the binary collision mechanism (i.e. nearly free electron scattering from the projectile ion). In such a case, the collision between projectile ion and each individual atom is to be considered. It has been very well reproduced by both CDW-EIS and CB1 calculations. For CDW-EIS, it is well understood as it takes in to account for both the projectile and target fields. It is also expected for the CB1 as the calculation is based on the first Born approximation. The electron emission cross section in the forward direction is higher as compared to the backward direction for high energy electrons. The forward–backward asymmetry arises due to the post-collision projectile interaction with the emitted electrons. For higher energy electrons, CB1 calculation largely overestimates the forward–backward asymmetry. The CB1 calculation uses Salin’s factor to take in to account the PCI effect [43, 63]. The CDW-EIS calculation reproduces the asymmetry reasonably well for intermediate energy electrons. However, for high energy electrons, it also overestimates the asymmetry. This has been discussed in

more detail by looking into the forward–backward asymmetry parameter in section 4.4.

#### 4.2. SDCS and TCS

The SDCS, the differential in the energy (angle) is obtained by numerically integrating the DDCS data over the emission angles (energies). For the energy distribution, the DDCS data is integrated in the angular range of 20°–160°. The angular distribution is obtained by integrating the DDCS data over the range of 5 eV–400 eV.

$$\frac{d\sigma}{d\varepsilon_e} = \int \frac{d^2\sigma}{d\Omega_e d\varepsilon_e} d\Omega_e, \quad (9)$$

$$\frac{d\sigma}{d\Omega_e} = \int \frac{d^2\sigma}{d\Omega_e d\varepsilon_e} d\varepsilon_e,$$

where  $\sigma$  is the total electron emission cross section,  $\varepsilon_e$  is the emitted electron energy and  $\Omega_e$  is the solid angle of electron emission.

The energy and angular distribution of SDCS are plotted in figure 6. The solid (blue) and dashed (black) curves in figure 6 represent the CDW-EIS and CB1 calculations respectively. The energy distribution (see figure 6(a)) grossly shows similar features like that for DDCS at individual angles. The C-KLL Auger peak is clearly visible around 240 eV. Overall the CB1 calculation largely underestimates the cross section except for low energy electrons ( $\leq 9$  eV). The deviation from the measured data increases with increasing electron energies. In comparison to the CB1, the CDW-EIS is in better agreement with the data. However, it also overestimates the data for low energy electrons but predicts the data reasonably well for intermediate and high energy electrons.

The angular distribution (see figure 6(b)) shows significantly different behavior than that predicted by the CB1 calculation. The CB1 calculation shows a peak like structure around 80° due to binary encounter collision but the data shows near-constant behavior for the forward angles. Also, we have observed a fairly large forward–backward asymmetry in the angular SDCS whereas calculations fail to predict such asymmetry. The difference between the CB1 and the experimental data of  $d\sigma/d\Omega_e$ , particularly in the forward angle needs more attention. As far as the CDW-EIS model is concerned, overall it overestimates the data at all the angles. However, it provides a very good qualitative agreement with the data. Moreover, it very well reproduces the forward–backward asymmetry.

We have also obtained a TCS by numerically integrating DDCS over both the electron energies and the emission angles in the range of 5 eV–400 eV and 20°–160° respectively. The TCS for electron emission is found to be  $1.0 \times 10^{-14}$  cm<sup>2</sup>. The TCS predicted by the CDW-EIS for the same energy and angular range is  $1.26 \times 10^{-14}$  cm<sup>2</sup> which is in reasonable agreement with the experiment. Whereas that predicted by the CB1 calculation is  $4.84 \times 10^{-15}$  cm<sup>2</sup> which is an underestimation by a factor of 2.1. The TCS has also been derived for the entire angular range (0°–180°). The missing data below 20° and above 160° have been obtained by extrapolating the measured data based on the distribution for CDW-EIS calculations. The SDCS value at 0° has been assumed to be the same as 20°



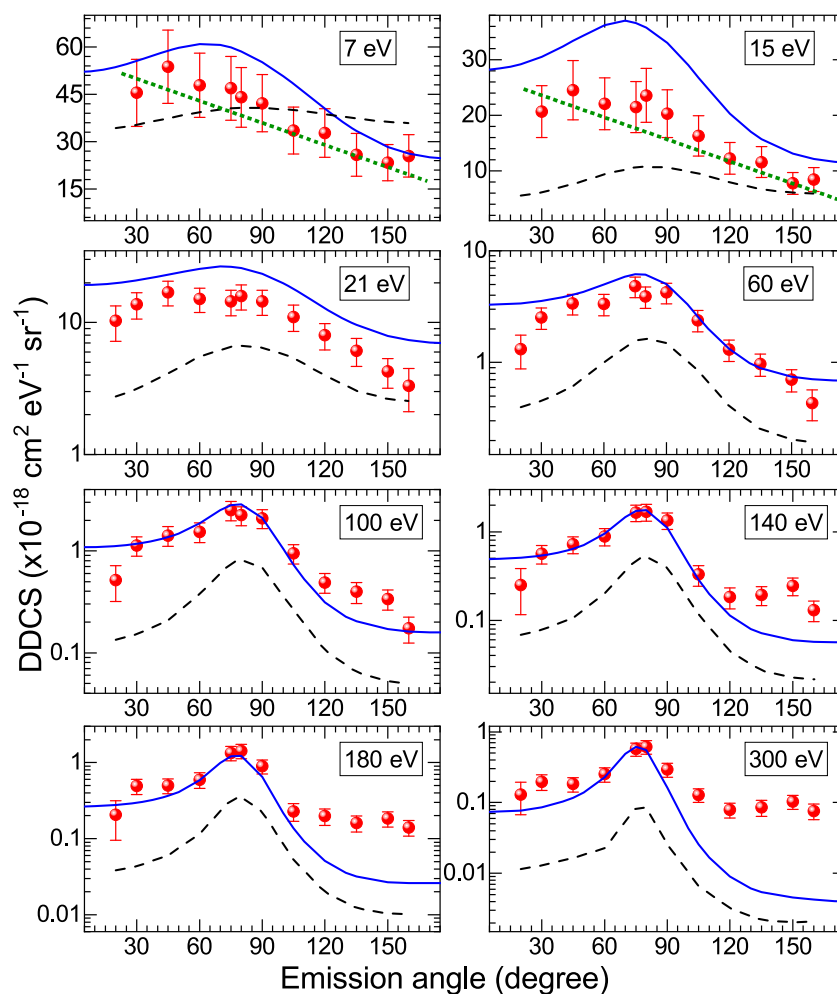


**Figure 5.** Angular distributions of DDCS of electron emission from fluorene (filled circles) for different electron emission energies as indicated in panels. Solid (blue) line and dashed (black) lines represent the CDW-EIS and CB1 calculations respectively. The dotted (green) line is guide to the eye.

and similarly at  $180^\circ$  to be the same as  $160^\circ$ , as, the CDW-EIS has nearly flat distribution. The contribution of these angles to the TCS is about 4.5%. The ratio of the total measured cross section for fluorene and  $\text{CH}_4$  molecules is 7.9. The ratio of the number of valence electrons in fluorene to  $\text{CH}_4$  is 7.75, since, the number of valence electrons in fluorene is 62 and in  $\text{CH}_4$  it is 8. Hence, the total electron emission cross section from fluorene molecule scales reasonably well according to the valence electron scaling.

#### 4.3. C-KLL Auger and hyper-satellite

The observed C-KLL Auger electron peak, around 240 eV, in the energy distribution of electron emission has been studied in detail by looking into its angular distribution. The Auger cross section has been obtained by integrating the area under the curve. The resulting angular distribution is found to show some variation (see figure 7). Since the KLL Auger electron arises because of the K-shell vacancy, the angular distribution is dependent upon the final state symmetry of the molecule. Particularly for atomic targets, it has been observed that the KLL Auger electron shows near isotropic distribution [25, 64].

Some deviation from isotropic distribution has previously been observed and explained in terms of beam alignment effects and the multiple L-shell vacancy production [32, 65–68]. TCS for the C-KLL Auger electron emission from fluorene is found to be  $2.91 \times 10^{-16} \text{ cm}^2$ .

In the case of the heavy-ion projectile, the probability of double K-vacancy production in the target can be considerable. We observe a shoulder in the C-KLL Auger peak, the hyper-satellite peak, corresponding to the double K-vacancy production in the target. The area under the hyper-satellite peak has been obtained by fitting both Auger and hyper-satellite peak simultaneously. The hyper-satellite is mainly studied for backward angles as the extraction of its contribution for the forward angles was difficult due to the large Coulomb background. The electron emission cross section has been integrated over the backward angles in the range  $120^\circ$ – $160^\circ$ . The integrated cross section along with the peak fits are shown in figure 8. For the integrated cross section over the backward angles, the hyper-satellite and the Auger electron emission cross sections are obtained from the fit. The ratio of double to single K-vacancy production is found to be about 8.6%.

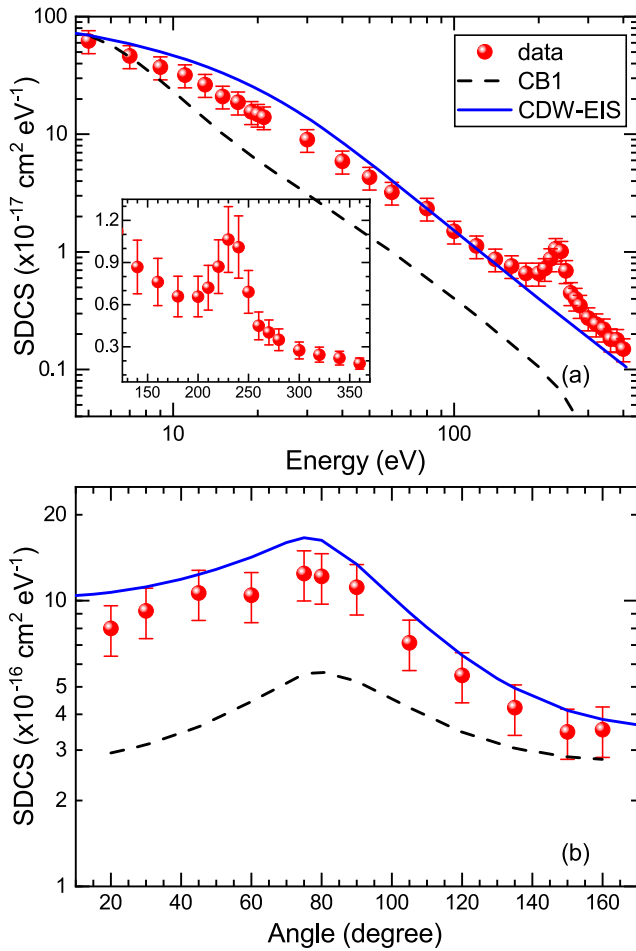


**Figure 6.** Energy and angular distributions of SDCS of electron emission from fluorene upon 98 MeV Si<sup>8+</sup> ion impact. Solid (blue) and dashed (black) lines represent the CDW-EIS and CB1 calculations respectively.

#### 4.4. Asymmetry parameter

As we have seen in previous sections, the electron emission cross section is large in the forward direction as compared to the backward direction. The forward–backward asymmetry in electron emission arises mainly due to two factors [69], (a) PCI of the electron with both the residual target and the projectile ion and (b) non-Coulombic potential of the multi-electronic system. The forward–backward asymmetry differs for different targets and hence it can provide a better understanding of the collision mechanism involved. Hence, to quantify this as a function of ejected electron energy, we have plotted a forward–backward asymmetry parameter,  $\alpha(\varepsilon_e, \theta)$ , defined as follow,

$$\alpha(\varepsilon_e, \theta) = \frac{\sigma(\varepsilon_e, \theta) - \sigma(\varepsilon_e, \pi - \theta)}{\sigma(\varepsilon_e, \theta) + \sigma(\varepsilon_e, \pi - \theta)}, \quad (10)$$

where  $\varepsilon_e$  is the electron energy,  $\theta$  is a forward electron emission angle, and  $\sigma(\varepsilon_e, \theta)$  corresponds to the e-DDCS values at electron energy  $\varepsilon_e$ , and at an angle  $\theta$ .

The forward–backward asymmetry parameter is plotted in the electron energy range of 7 eV–150 eV, for two sets of forward–backward angles in figure 9 along with the prediction

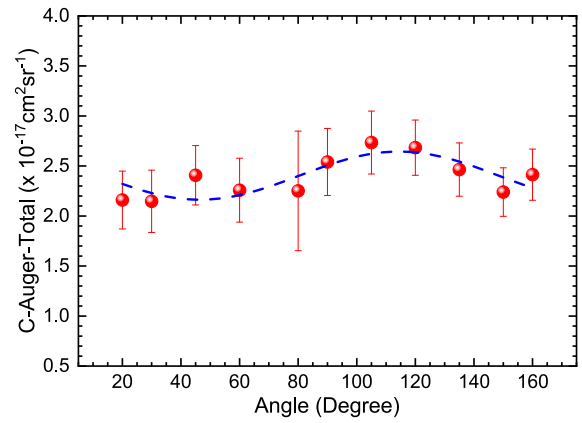


**Figure 7.** Angular distribution of the C-KLL Auger electron emission cross section for fluorene molecules. The dashed line represents the guide to the eye.

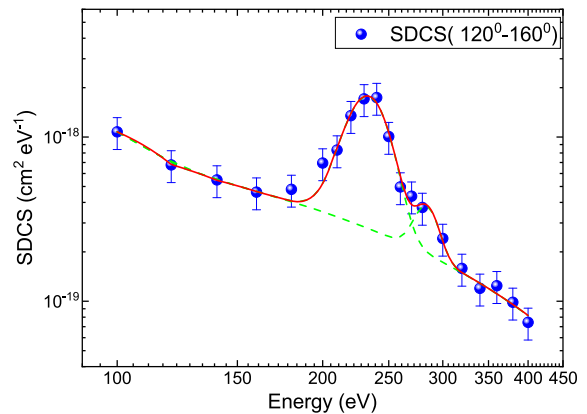


**Figure 8.** Integrated electron emission cross section over the backward angles in the range 120°–160°. The solid (red) and dashed (green) lines represent the cumulative peak fit and the individual peak fits respectively.

of the CDW-EIS (solid line) and the CB1 (dashed line) calculation. The experimental data for the CH<sub>4</sub> molecule (open triangle) is also plotted along with the fluorene data. The CH<sub>4</sub> data are normalized to the fluorene data at 19 eV. The CH<sub>4</sub> target has a higher forward–backward asymmetry and hence the normalization constants for panel (a) is 0.7 and that for panel (b) is 0.75. In general, the forward–backward asymmetry parameter is lowest for the low energy electrons and then increases with the ejected electron energy. For the CH<sub>4</sub> target, the asymmetry increases monotonically without any peak. It can also be understood in terms of the PCI effect which is quite small for the lowest energy electrons as these electrons are emitted in a large impact parameter collisions. Also the large separation between the fast moving projectiles and the slow electrons reduces the PCI effect. These are well understood and is built in the CDW-EIS model which gives a good agreement with the data except at lowest energy region where one finds broad peak-like structure in the experimental data.

However, the CDW-EIS model predicts the usual molecular behavior reasonably well for the fluorene target up to 30 eV.

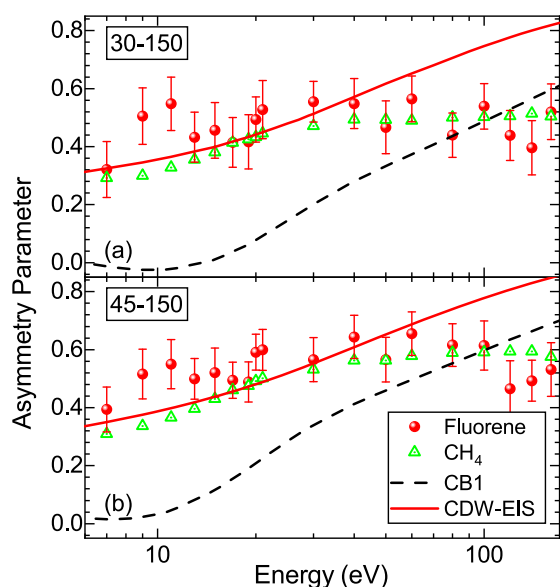


**Figure 9.** Forward–backward asymmetry parameter for  $e^-$ -emission from fluorene (solid circles) as a function of ejected electron energy, along with the CDW-EIS (solid red line) and CB1 (dashed black line) model prediction. The open triangles shows the data for  $\text{CH}_4$ .

For the electrons above 30 eV, the forward–backward asymmetry has a constant value in contrast to the CDW-EIS model prediction of the increasing asymmetry. In CB1 calculations, the Salin’s factor is used to incorporate the effect of both the projectile and residual target interaction (TCEE). The Salin’s factor describes the density of the continuum states associated with the electron–projectile interaction. The CB1 calculation shows a large discrepancy in terms of both qualitative and quantitative predictions. The discrepancy with the theory indicates the influence of the molecular structure in electron emissions. Hence, it is important to improve the Salin’s factor in case of a large molecular target, such as, fluorene.

The broad peak-like structure around 11 eV could possibly be indicative of plasmon excitation, in line with earlier investigations [23, 24] but can not be confirmed here due to relatively large uncertainties in the data points. Such a giant plasmon resonance peak [42] in the asymmetry parameter has been observed in case of a bigger PAH molecule, such as, coronene [23, 24]. Perhaps projectiles with higher perturbation strength,  $Z_p/v$ , is required to excite the plasmon resonance for such relatively smaller PAH molecule, fluorene. Such an experiment is in progress.

## 5. Conclusions

We have measured the absolute DDCS of electron emission from a PAH molecule, fluorene, upon 3.5 MeV/u  $\text{Si}^{8+}$  ion impact. The measured energy and angular distributions of the  $e^-$ -emission have been compared with the CDW-EIS and the CB1 model calculations. Overall, the CB1 calculation largely underestimates the cross sections. Nevertheless, it is successful in reproducing some of the features, such as a peak in angular distribution due to the binary nature of the collision. On the

other hand, the CDW-EIS calculations which has been applied for the first time for a PAH molecule, show much better overall agreement with the data. As far as the forward–backward angular asymmetry is concerned the CDW-EIS explains the data much better compared to the CB1 calculations. Certain improvement in the CB1 model for such large molecules can be predicted from these data. The angular distribution of the C-KLL Auger cross section show certain variation in contrast to the isotropic behavior as expected for atomic targets. The double K-vacancy production cross section is found to be 8.6% of the single K-vacancy production. Both the single differential distributions (i.e.  $d\sigma/d\Omega_e$  and  $d\sigma/d\varepsilon_e$ ) and the TCS of electron emission are in good agreement with the CDW-EIS model. The total cross sections for the methane and fluorene scale reasonably well according to the valence electron scaling. The forward–backward angular asymmetry shows relatively flatter distribution compared to the theoretical predictions and the CDW-EIS provides a better qualitative agreement compared to the CB1. The giant plasmon excitation could not be clearly observed in the asymmetry parameter, although there exist a mild indication.

## Acknowledgments

Authors would like to acknowledge Pelletron accelerator staff for smooth running of the machine. We thank Nilesh Mhatre, W A Fernandes, Thulasi Ram and S N Manjarekar for their technical support. The support of the Department of Atomic Energy, Government of India, under Project No. 12P-R & D-TFR-5.02-0300 is acknowledged. L G acknowledges support from the Hungarian Scientific Research Fund (Grant No. K 128621). Sandia National Laboratories is a multi-mission laboratory managed and operated by National Technology and Engineering Solutions of Sandia, LLC., a wholly owned subsidiary of Honeywell International, Inc., for the US Department of Energy’s National Nuclear Security Administration under Contract DE-NA0003525. The views expressed in the article do not necessarily represent the views of the US DOE or the United States Government.

## Data availability statement

The data that support the findings of this study are available upon reasonable request from the authors.

## ORCID iDs

Chandan Bagdia  <https://orcid.org/0000-0003-4647-6023>  
 Deepankar Misra  <https://orcid.org/0000-0001-6048-3444>  
 Lokesh C Tribedi  <https://orcid.org/0000-0002-9282-9734>

## References

- [1] Tielens A G G M 2013 *Rev. Mod. Phys.* **85** 1021–81
- [2] Feng X, Pisula W and Müllen K 2009 *Pure Appl. Chem.* **81** 2203–24

- [3] Simpson C D, Brand J D, Berresheim A J, Przybilla L, Räder H J and Müllen K 2002 *Chem. Eur. J.* **8** 1424–9
- [4] Allamandola L J, Hudgins D M and Sandford S A 1999 *Astrophys. J.* **511** L115–9
- [5] Henning T and Salama F 1998 *Science* **282** 2204–10
- [6] Leger A and D'Hendecourt L 1985 *Astron. Astrophys.* **146** 81–5  
<https://ui.adsabs.harvard.edu/abs/1985A&A...146...81L>
- [7] Boschi R, Clar E and Schmidt W 1974 *J. Chem. Phys.* **60** 4406–18
- [8] Bakes E L O and Tielens A G G M 1994 *Astrophys. J.* **427** 822
- [9] Bakes E L O and Tielens A G G M 1998 *Astrophys. J.* **499** 258–66
- [10] Micelotta E R, Jones A P and Tielens A G G M 2010 *Astron. Astrophys.* **510** A36
- [11] Micelotta E R, Jones A P and Tielens A G G M 2011 *Astron. Astrophys.* **526** A52
- [12] Xiang F Y, Li A and Zhong J X 2011 *Astrophys. J.* **733** 91
- [13] James L 2005 *The Interstellar Medium* (Berlin: Springer) ch 6 pp 119–48
- [14] Holm A I S et al 2010 *Phys. Rev. Lett.* **105** 213401
- [15] Ławicki A et al 2011 *Phys. Rev. A* **83** 022704
- [16] Martin S, Chen L, Brédy R, Montagne G, Ortega C, Schlathöler T, Reitsma G and Bernard J 2012 *Phys. Rev. A* **85** 052715
- [17] Mishra P M, Rajput J, Safvan C P, Vig S and Kadhane U 2014 *J. Phys. B: At. Mol. Opt. Phys.* **47** 085202
- [18] Postma J, Bari S, Hoekstra R, Tielens A G G M and Schlathöler T 2009 *Astrophys. J.* **708** 435–44
- [19] Reitsma G, Zettergren H, Martin S, Brédy R, Chen L, Bernard J, Hoekstra R and Schlathöler T 2012 *J. Phys. B: At. Mol. Opt. Phys.* **45** 215201
- [20] Reitsma G, Zettergren H, Boschman L, Bodewits E, Hoekstra R and Schlathöler T 2013 *J. Phys. B: At. Mol. Opt. Phys.* **46** 245201
- [21] Rousseau P et al 2012 *Nucl. Instrum. Methods Phys. Res. B* **279** 140–3
- [22] Gatchell M and Zettergren H 2016 *J. Phys. B: At. Mol. Opt. Phys.* **49** 162001
- [23] Biswas S and Tribedi L C 2015 *Phys. Rev. A* **92** 060701
- [24] Biswas S, Champion C, Weck P F and Tribedi L C 2017 *Sci. Rep.* **7** 5560
- [25] Biswas S, Misra D, Monti J M, Tachino C A, Rivarola R D and Tribedi L C 2014 *Phys. Rev. A* **90** 052714
- [26] Biswas S, Kasthurirangan S, Misra D, Monti J M, Rivarola R D, Fainstein P D and Tribedi L C 2015 *Phys. Rev. A* **91** 022711
- [27] Biswas S, Monti J M, Tachino C A, Rivarola R D and Tribedi L C 2015 *J. Phys. B: At. Mol. Opt. Phys.* **48** 115206
- [28] Nandi S, Biswas S, Tachino C A, Rivarola R D and Tribedi L C 2015 *Eur. Phys. J. D* **69** 192
- [29] Nandi S, Biswas S, Khan A, Monti J M, Tachino C A, Rivarola R D, Misra D and Tribedi L C 2013 *Phys. Rev. A* **87** 052710
- [30] Bhattacharjee S et al 2016 *J. Phys. B: At. Mol. Opt. Phys.* **49** 065202
- [31] Bhattacharjee S, Biswas S, Monti J M, Rivarola R D and Tribedi L C 2017 *Phys. Rev. A* **96** 052707
- [32] Bhattacharjee S, Bagdia C, Chowdhury M R, Monti J M, Rivarola R D and Tribedi L C 2018 *Eur. Phys. J. D* **72** 15
- [33] Agnihotri A N et al 2012 *Phys. Rev. A* **85** 032711
- [34] Agnihotri A N, Nandi S, Kasthurirangan S, Kumar A, Galassi M E, Rivarola R D, Champion C and Tribedi L C 2013 *Phys. Rev. A* **87** 032716
- [35] Agnihotri A N et al 2013 *J. Phys. B: At. Mol. Opt. Phys.* **46** 185201
- [36] Champion C, Galassi M E, Weck P F, Incerti S, Rivarola R D, Fojón O, Hanssen J, Iriki Y and Itoh A 2013 *Nucl. Instrum. Methods Phys. Res. B* **314** 66–70
- [37] Itoh A, Iriki Y, Imai M, Champion C and Rivarola R D 2013 *Phys. Rev. A* **88** 052711
- [38] Lüdde H J, Achenbach A, Kalkbrenner T, Jankowiak H-C and Kirchner T 2016 *Eur. Phys. J. D* **70** 82
- [39] Gutfreund H and Little W A 1969 *J. Chem. Phys.* **50** 4478–85
- [40] Ling Y and Lifshitz C 1996 *Chem. Phys. Lett.* **257** 587–91
- [41] Jochims H W, Rühl E, Baumgärtel H, Tobita S and Leach S 1997 *Int. J. Mass Spectrom. Ion Process.* **167–168** 35–53
- [42] Verkhovtsev A V, Korol A V and Solov'yov A V 2014 *J. Phys.: Conf. Ser.* **490** 012159
- [43] Champion C, Lekadir H, Galassi M E, Fojón O, Rivarola R D and Hanssen J 2010 *Phys. Med. Biol.* **55** 6053–67
- [44] Gulyás L, Tóth I and Nagy L 2013 *J. Phys. B: At. Mol. Opt. Phys.* **46** 075201
- [45] Misra D, Thulasiram K V, Fernandes W, Kelkar A H, Kadhane U, Kumar A, Singh Y, Gulyás L and Tribedi L C 2009 *Nucl. Instrum. Methods Phys. Res. B* **267** 157–62
- [46] Sigma-Aldrich <https://sigmaaldrich.com/catalog/product/aldrich/128333> (accessed 27 July 2019)
- [47] Verevkin S P 2004 *Fluid Phase Equilib.* **225** 145–52
- [48] Scoles G 1988 *Atomic and Molecular Beam Methods* vol 1 ed G Scoles, D Bassi, U Buck and D Laine (Oxford: Oxford University Press) ch 4 pp 83–90
- [49] Bagdia C, Bhattacharjee S, Roychowdhury M, Mandal A, Lapicki G and Tribedi L C 2020 *X-Ray Spectrom.* **49** 160–4
- [50] Belkic D, Gayet R, Hanssen J and Salin A 1986 *J. Phys. B: At. Mol. Phys.* **19** 2945–53
- [51] Frisch M et al 2009 GAUSSIAN 09 (Revision A.02) Wallingford, CT Gaussian, Inc.
- [52] Crothers D S F and Dubé L J 1992 *Continuum Distorted Wave Methods in Ion—Atom Collisions (Advances in Atomic, Molecular, and Optical Physics)* vol 30 ed D Bates and B Bederson (New York: Academic) pp 287–337
- [53] Stolterfoht N, DuBois R D and Rivaola R D 1997 *Electron Emission in Heavy Ion Atom Collision* (Berlin: Springer)
- [54] Tachino C A, Monti J M, Fojón O A, Champion C and Rivarola R D 2014 *J. Phys. B: At. Mol. Opt. Phys.* **47** 035203
- [55] Belkic D, Gayet R and Salin A 1979 *Phys. Rep.* **56** 279–369
- [56] Gulyás L, Fainstein P D and Salin A 1995 *J. Phys. B: At. Mol. Opt. Phys.* **28** 245–57
- [57] Pople J A and Segal G A 1966 *J. Chem. Phys.* **44** 3289–96
- [58] Mulliken R S 1949 *J. Chim. Phys.* **46** 675–713
- [59] Dreizler R M and Gross E K U 1990 *Density Functional Theory* (Berlin: Springer)
- [60] Dunning T H 1989 *J. Chem. Phys.* **90** 1007–23
- [61] Champion C 2013 *J. Chem. Phys.* **138** 184306
- [62] Gulyás L, Egri S, Ghavamnia H and Igarashi A 2016 *Phys. Rev. A* **93** 032704
- [63] Salin A 1969 *J. Phys. B: At. Mol. Phys.* **2** 631–9
- [64] Kobayashi N, Irie T, Maeda N, Kojima H, Akanuma S-i and Sakisaka M 1979 *J. Phys. Soc. Japan* **47** 234–9
- [65] Stolterfoht N, Schneider D, Burch D, Aagaard B, Bøving E and Fastrup B 1975 *Phys. Rev. A* **12** 1313–29
- [66] Hemmers O, Heiser F, Eiben J, Wehlitz R and Becker U 1993 *Phys. Rev. Lett.* **71** 987–90
- [67] Dill D, Swanson J R, Wallace S and Dehmer J L 1980 *Phys. Rev. Lett.* **45** 1393–6
- [68] Berezhko E G and Kabachnik N M 1977 *J. Phys. B: At. Mol. Phys.* **10** 2467–77
- [69] Fainstein P D, Gulyás L, Martín F and Salin A 1996 *Phys. Rev. A* **53** 3243–6